#### **OPEN ACCESS**



## The Kelvin-Helmholtz Instability at the Boundary of Relativistic Magnetized Jets

Anthony Chow 10, Jordy Davelaar 1,20, Michael E. Rowan 30, and Lorenzo Sironi 10

Department of Astronomy and Columbia Astrophysics Laboratory, Columbia University, New York, NY 10027, USA; kc3058@columbia.edu, jrd2210@columbia.edu, lsironi@astro.columbia.edu

Center for Computational Astrophysics, Flatiron Institute, 162 Fifth Avenue, New York, NY 10010, USA

Advanced Micro Devices, Inc., Santa Clara, CA, USA; michael.rowan@amd.com

#### Abstract

Received 2023 March 13; revised 2023 June 15; accepted 2023 June 20; published 2023 July 7

We study the linear stability of a planar interface separating two fluids in relative motion, focusing on conditions appropriate for the boundaries of relativistic jets. The jet is magnetically dominated, whereas the ambient wind is gaspressure-dominated. We derive the most general form of the dispersion relation and provide an analytical approximation of its solution for an ambient sound speed much smaller than the jet Alfvén speed  $v_A$ , as appropriate for realistic systems. The stability properties are chiefly determined by the angle  $\psi$  between the wavevector and the jet magnetic field. For  $\psi = \pi/2$ , magnetic tension plays no role, and our solution resembles the one of a gas-pressure-dominated jet. Here, only sub-Alfvénic jets are unstable  $(0 < M_e \equiv (v/v_A)\cos\theta < 1$ , where v is the shear velocity and  $\theta$  the angle between the velocity and the wavevector). For  $\psi = 0$ , the free energy in the velocity shear needs to overcome the magnetic tension, and only super-Alfvénic jets are unstable  $(1 < M_e < \sqrt{(1 + \Gamma_w^2)/[1 + (v_A/c)^2\Gamma_w^2]},$  with  $\Gamma_w$  the wind adiabatic index). Our results have important implications for the propagation and emission of relativistic magnetized jets.

*Unified Astronomy Thesaurus concepts:* Plasma astrophysics (1261); Plasma jets (1263); High energy astrophysics (739); Relativistic jets (1390); Magnetohydrodynamics (1964); Relativistic fluid dynamics (1389)

#### 1. Introduction

The Kelvin-Helmholtz instability (KHI; Von Helmholtz & Monats 1868; Lord Kelvin 1871)—at the interface of two fluids in relative motion—is one of the most ubiquitous and wellstudied instabilities in the universe. Since the pioneering works of Chandrasekhar (1961), the linear theory of the KHI has been investigated under a variety of conditions (Blumen et al. 1975; Blandford & Pringle 1976; Turland & Scheuer 1976; Ferrari et al. 1978, 1980; Pu & Kivelson 1983; Kivelson & Zu-Yin 1984; Sharma & Chhajlani 1998; Bodo et al. 2004, 2013, 2016, 2019; Osmanov et al. 2008; Prajapati & Chhajlani 2010; Hamlin & Newman 2013; Sobacchi & Lyubarsky 2018; Berlok & Pfrommer 2019; Pimentel & Lora-Clavijo 2019; Rowan 2019), depending on whether the relative motion is nonrelativistic or ultrarelativistic, whether the two fluids have comparable or different properties (respectively, "symmetric" or "asymmetric" configuration), whether the flow is incompressible or compressible, and whether or not the fluids are magnetized.

The boundaries of relativistic astrophysical jets may be prone to the KHI, given the relative (generally, ultrarelativistic) shear velocity between the jet and the ambient medium (hereafter, the "wind"). In jet boundaries with flow-aligned magnetic fields, KH vortices can wrap up the field lines onto themselves, leading to particle acceleration via reconnection (Rowan 2019; Sironi et al. 2021). Particles pre-energized by reconnection (e.g., Sironi & Spitkovsky 2014; Zhang et al. 2021; Sironi 2022) can then experience shear-driven acceleration (Rieger 2019; Wang et al. 2021, 2023)—i.e., particles scatter in between regions that move toward each other because

Original content from this work may be used under the terms of the Creative Commons Attribution 4.0 licence. Any further distribution of this work must maintain attribution to the author(s) and the title of the work, journal citation and DOI.

of the velocity shear, akin to the Fermi process in converging flows (Fermi 1949). The KHI may then constitute a fundamental building block for our understanding of the origin of radio-emitting electrons in limb-brightened relativistic jets (e.g., in Cygnus A—Boccardi et al. 2016; and in M87—Walker et al. 2018), and for the prospects of shear-driven acceleration at jet boundaries in generating ultra-high-energy cosmic rays.

A study of the KHI in this context needs to account for the unique properties of the boundaries of relativistic jets. First, the relative motion between the jet and the wind can be ultrarelativistic; second, while the wind is likely gas-pressure-dominated, relativistic jets are believed to be magnetically dominated (Blandford & Znajek 1977), i.e., an asymmetric configuration. The linear stability properties of the KHI in this regime (of relativistic, asymmetric, magnetized flows) are still unexplored. In this letter, we derive the most general form of the dispersion relation for the KHI at the interface between a magnetized relativistic jet and a gas-pressure-dominated wind. We also provide an analytical approximation of its solution for wind sound speeds much smaller than the jet Alfvén speed, as appropriate for realistic astrophysical systems.

### 2. Setup

We consider a planar vortex sheet interface in the x-z plane at y=0, as shown in Figure 1. The jet (y>0) is cold and magnetized, with field  $\mathbf{B}_{0j}=(B_{0x},\,0,\,B_{0z})$  lying in the x-z plane and Alfvén speed  $v_{\rm A}$ . The abilient wind (y<0) is gas-pressure-supported (with sound speed  $c_{\rm sw}$ ) and has a vanishing magnetic field. We use the subscript "j" for the jet and "w" for the wind. We solve the system in the jet rest frame, where the wind moves with velocity  $\mathbf{v}=v~\hat{x}$ . We adopt Gaussian units such that  $c=4~\pi=1$  and define all velocities in units of c.

We describe the flow with the equations of relativistic magnetohydrodynamics (RMHDs; e.g., Mignone et al. 2018;

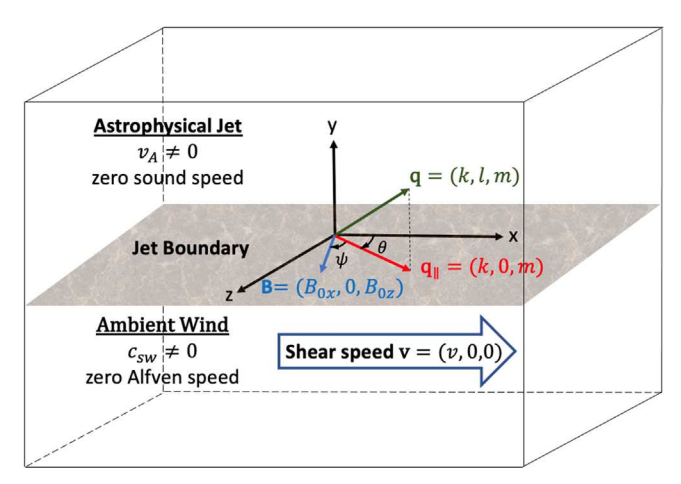


**Figure 1.** A 3D schematic diagram of the boundary of the relativistic jet. The boundary (gray color) is located in the x-z plane. Above and below the boundary are the magnetically dominated cold jet and the unmagnetized gaspressure-supported ambient wind, respectively.  $q_{\parallel}$  is the projection of the wavevector q onto the boundary. The jet is at rest and the wind has a relative shear speed of  $\nu$ . The magnetic field in the jet is B.  $\theta$  is the angle between  $q_{\parallel}$  and  $\nu$ , while  $\psi$  is the angle between B and  $q_{\parallel}$ .

Rowan 2019):

$$\frac{\partial(\rho\gamma)}{\partial t} + \nabla \cdot (\rho\gamma \mathbf{v}) = 0, \tag{1a}$$

$$\frac{\partial}{\partial t}(w\gamma^2 \mathbf{v}) + \nabla \cdot (w\gamma^2 \mathbf{v}\mathbf{v}) + \nabla p = \rho_e \mathbf{E} + \mathbf{J} \times \mathbf{B}, \quad (1b)$$

$$\frac{\partial \mathbf{B}}{\partial t} + \nabla \times \mathbf{E} = 0, \tag{1c}$$

$$\frac{\partial \mathbf{E}}{\partial t} - \nabla \times \mathbf{B} = -\mathbf{J},\tag{1d}$$

$$\frac{\partial}{\partial t}(w\gamma^2 - p) + \nabla \cdot (w\gamma^2 \mathbf{v}) = \mathbf{J} \cdot \mathbf{E}, \tag{1e}$$

supplemented with the divergence constraints

$$\nabla \cdot \mathbf{E} = \rho_{e}, \quad \nabla \cdot \mathbf{B} = 0. \tag{2}$$

Here,  $\rho$ ,  $\rho_e$ , J, v,  $\gamma$ , B, E, w, and p are the rest-mass density, charge density, current density, fluid velocity, Lorentz factor  $(\gamma = 1/\sqrt{1-v^2})$ , magnetic field, electric field, gas enthalpy density, and pressure, respectively. For an ideal gas with adiabatic index  $\Gamma$ , the enthalpy can be written as  $w = \rho + \Gamma p/(\Gamma - 1)$ .

We assume a cold and magnetically dominated jet, with Alfvén speed  $v_A^2 = v_{A,in}^2 + v_{A,out}^2$ , where

$$v_{\text{A,in}} = \sqrt{\frac{B_{0x}^2}{w_{0j} + B_{0x}^2 + B_{0z}^2}}, v_{\text{A,out}} = \sqrt{\frac{B_{0z}^2}{w_{0j} + B_{0x}^2 + B_{0z}^2}}$$
 (3)

and the jet enthalpy density is  $w_{0j} \approx \rho_{0j}$  for a cold jet. The wind has negligible magnetic field and is gas-pressure-supported, with sound speed (Mignone et al. 2018)

$$c_{\rm sw} = \sqrt{\frac{w_{0w} - \rho_{0w}(\partial w_{0w}/\partial \rho_{0w})}{(\partial w_{0w}/\partial \rho_{0w}) - 1} \frac{1}{w_{0w}}} = \sqrt{\Gamma_w \frac{p_{0w}}{w_{0w}}}, \quad (4)$$

where  $w_{0w}$  is the wind enthalpy density. From pressure balance across the interface.

$$\frac{1}{2}(B_{0x}^2 + B_{0z}^2) = \frac{c_{\text{sw}}^2 w_{0w}}{\Gamma_w} \Rightarrow \frac{w_{0w}}{w_{0i}} = \frac{1}{2} \frac{v_A^2 \Gamma_w}{(1 - v_A^2) c_{\text{sw}}^2}, \quad (5)$$

where  $\Gamma_w$  is the wind adiabatic index.

#### 3. Dispersion Relation

The dispersion relation of surface waves at the interface can be found from the dispersion relations of body waves in both the jet and the ambient wind, together with the displacement matching at the interface. The dispersion relations of body waves in each of the two fluids can be found by linearizing Equation (1), such that the perturbed variables take the form  $\varphi \approx \varphi_0 + \varphi_1$ , where  $\varphi_0$  and  $\varphi_1$  are the background and the first-order perturbed variables respectively. The perturbed electric field in the jet is  $E_1 = -v_1 \times B_{0j}$  in the ideal MHD limit, where  $v_1$  is the perturbed velocity in the jet frame.

$$\cos \theta = \frac{k}{\sqrt{k^2 + m^2}}. (6)$$

Similarly, we define the angle  $\psi$  between the wavevector projection onto the x-z plane and the jet magnetic field such that

$$\cos \psi = \frac{k v_{\text{A,in}} + m v_{\text{A,out}}}{v_{\text{A}} \sqrt{k^2 + m^2}}.$$
 (7)

For a magnetized cold jet, the dispersion relation of its body waves describes magnetosonic waves in the cold plasma limit:

$$\omega[\omega^2 - (kv_{A,in} + mv_{A,out})^2]$$
  

$$[\omega^2 - (k^2 + l_i^2 + m^2)v_A^2] = 0.$$
 (8)

In the wind, we consider perturbed variables  $\varphi_1$  of the form  $\varphi_1 \propto e^{i(\tilde{q}\cdot x - \tilde{\omega}t)}$ , where  $\tilde{q} = (\tilde{k}, l_w, m)$  is the complex wavevector and  $\tilde{\omega}$  is the complex angular frequency, both defined in the wind rest frame. For an unmagnetized wind, the dispersion relation of its body waves reduces to the one of sound waves,  $\tilde{\omega}^2 - (\tilde{k}^2 + l_w^2 + m^2)c_{\rm sw}^2 = 0$ . By Lorentz transformations of  $\tilde{\omega} = \gamma(\omega - kv)$  and  $\tilde{k} = \gamma(k - v\omega)$ , we obtain

$$\gamma^2(\omega - kv)^2 = c_{\text{sw}}^2 [l_w^2 + m^2 + \gamma^2 (k - \omega v)^2].$$
 (9)

Since  $l_j$  and  $l_w$  are Lorentz invariant, by solving Equations (8) and (9) for  $l_j$  and  $l_w$ , respectively, we can construct a Lorentz-invariant ratio:

$$\frac{l_w^2}{l_i^2} = \frac{v_A^2 \left[\gamma^2 (\omega - kv)^2 - c_{sw}^2 (m^2 + \gamma^2 (k - \omega v)^2)\right]}{c_{sw}^2 \left[\omega^2 - (k^2 + m^2)v_A^2\right]}.$$
 (10)

<sup>&</sup>lt;sup>4</sup> Resistive effects are likely important in the nonlinear stages (Sironi et al. 2021), but not for the linear analysis presented here.

An independent way of obtaining  $l_w/l_j$  is to simultaneously solve the linearized RMHD equation, Equation (1), together with the first-order pressure balance equation,

$$B_{0x}B_{1x} + B_{0z}B_{1z} = p_{1w}, (11)$$

and the displacement matching condition at the interface,

$$\frac{v_{1y,j}}{\omega} = \frac{v_{1y,w}}{\gamma(\omega - kv)},\tag{12}$$

yielding

$$\frac{l_w}{l_i} = \frac{\gamma^2 (1 - v_A^2)(\omega - kv)^2}{\omega^2 - (kv_{A,in} + mv_{A,out})^2} \frac{w_{0w}}{w_{0j}}.$$
 (13)

Using Equation (5), we can eliminate  $w_{0w}/w_{0j}$  from Equation (13) and, finally, the dispersion relation for the surface wave at the interface can be obtained by equating Equation (10) and the square of Equation (13):

$$\frac{\gamma^{2}(\omega - kv)^{2} - c_{\text{sw}}^{2}(m^{2} + \gamma^{2}(k - \omega v)^{2})}{\omega^{2} - (k^{2} + m^{2})v_{\text{A}}^{2}} \\
= \frac{1}{4} \frac{v_{\text{A}}^{2}\gamma^{4}(\omega - kv)^{4}\Gamma_{w}^{2}}{[\omega^{2} - (kv_{\text{A,in}} + mv_{\text{A,out}})^{2}]^{2}c_{\text{sw}}^{2}}.$$
(14)

By introducing the following notations,

$$\phi = \frac{\omega}{v_{\rm A}\sqrt{k^2 + m^2}}, \quad M = \frac{v}{v_{\rm A}}, \quad \epsilon = \frac{c_{\rm sw}}{v_{\rm A}}, \tag{15}$$

Equation (14) can be rewritten as (Sobacchi & Lyubarsky 2018; Rowan 2019)

$$4\epsilon^{2}(1 - M^{2}v_{A}^{2})(\cos^{2}\psi - \phi^{2})^{2}$$

$$[\epsilon^{2}(1 - 2Mv_{A}^{2}\phi\cos\theta + M^{2}v_{A}^{2}(\cos^{2}\theta - 1 + v_{A}^{2}\phi^{2}))$$

$$-(M\cos\theta - \phi)^{2}] = (M\cos\theta - \phi)^{4}(1 - \phi^{2})\Gamma_{w}^{2}.$$
(16)

The dispersion relation in Equation (16) holds for arbitrary values of  $c_{\rm sw}$ ,  $v_{\rm A}$ ,  $v_{\rm cos}\,\theta$ , and  $\cos\psi$ , subject only to the assumptions of a cold jet and an unmagnetized wind.

Since Equation (16) is a sextic equation in  $\phi$ , it has a total of six (generally, complex) roots. However, not all of them may be acceptable. First, not all of the solutions will satisfy Equation (13), since we have introduced spurious roots when squaring it. Also, by the Sommerfeld radiation condition (Sommerfeld 1912), only outgoing waves should be retained. This requires  $\text{Im}(l_w) < 0$  and  $\text{Im}(l_j) > 0$ . The expressions for  $l_w$  and  $l_j$  can be obtained from the derivation of Equation (13), so the Sommerfeld condition can be expressed as

$$\operatorname{Im}(l_w) = \operatorname{Im}\left(\frac{(\phi - M\cos\theta)^2}{\phi}\right) < 0, \tag{17a}$$

$$\operatorname{Im}(l_j) = \operatorname{Im}\left(\frac{\phi^2 - \cos^2 \psi}{\phi}\right) > 0. \tag{17b}$$

### 4. Analytical Approximation

Since in general a sextic equation has no algebraic roots (Abel 1826), only approximate solutions of  $\phi$  in Equation (16) can be obtained. We first note that the parameters in Equation (15) are chosen such that for a realistic wind with  $c_{\rm sw} \ll v_{\rm A}$ , we have  $\epsilon \ll 1$ , whereas the other parameters do not depend on  $c_{\rm sw}$ . We

then expand  $\phi$  as a power series of  $\epsilon$  of the form  $\phi \approx c_0 + c_1 \epsilon + c_2 \epsilon^2$ , where  $c_0$ ,  $c_1$ , and  $c_2$  are constant with respect to  $\epsilon$  and terms higher than  $\epsilon^2$  are ignored. Substituting this into Equation (16) and comparing coefficients of various powers of  $\epsilon$  on both sides, we can find an approximate solution for all six roots of Equation (16). If we define an effective Mach number,

$$M_e \equiv M \cos \theta = (v/v_A) \cos \theta,$$
 (18)

 $\mu \equiv \cos^2 \psi - M_e^2$ , and recognize that  $\gamma^{-2} = 1 - M^2 v_A^2$ , then the approximate roots that correspond to the unstable modes can be written as

$$\phi_{(M_e < 1)} = M_e + \Lambda_+ \epsilon - \Sigma_+ \epsilon^2, \tag{19}$$

$$\phi_{(M_{-}>1)} = M_e - \Lambda_- \epsilon + \Sigma_- \epsilon^2, \tag{20}$$

where

$$\Lambda_{\pm} = \sqrt{-\frac{2(\mu^2 \pm \lambda)}{\gamma^2 (1 - M_e^2) \Gamma_w^2}},$$
 (21)

$$\lambda = \sqrt{\mu^4 + \mu^2 (1 - M_e^2)(1 - M_e^2 v_A^2) \Gamma_w^2}.$$
 (22)

We find that the first-order term  $\Lambda_{\pm}\epsilon$  generally provides a good approximation of the numerical solution for  $\phi$ . However, the second-order term (which we write explicitly in Appendix B) is required for identifying the physical solutions that satisfy Equation (13) and the Sommerfeld condition. At zeroth order in  $\epsilon$ , the real part of the solution (i.e., the phase speed of unstable modes) is  $\phi = M_e$ , or equivalently  $\omega/k = v$ , i.e., unstable modes are purely growing in the wind frame.

In Figures 2 and 3, we compare the numerical solution (left column) of Equation (16) with our analytical approximation (right column). We fix  $c_{\rm sw}=0.005$  and consider  $v_{\rm A}=0.2$  and 0.8, so the assumption  $c_{\rm sw}/v_{\rm A}\ll 1$  of our analytical approximation is well satisfied. The analytical solution for  ${\rm Im}(\phi)$  displayed in the figures only employs the first-order terms (as discussed above, we also use the second-order terms to check the Sommerfeld constraint), yet it provides an excellent approximation of the numerical results, apart from  $M_e=1$ . For  $M_e=1$ , the first-order term  $\Lambda_\pm$  of our analytical approximation diverges. We discuss below this special case.

Our analytical approximation allows us to determine the range of  $M_e$  where the system is unstable. If  $\lambda$  in Equation (22) is imaginary, then also  $\Lambda_{\pm}$  has a nonzero imaginary part. We then find the values of  $M_e$  that satisfy  $\lambda^2=0$  and obtain the following unstable bounds: for  $M_e<1$ ,

$$\cos \psi < M_e < \min \left( \frac{\cos \theta}{\nu_{\rm A}}, 1 \right); \tag{23}$$

whereas for  $M_e > 1$ ,

$$\sqrt{\frac{\nu_1 - \nu_2}{2 + 2\nu_{\rm A}^2 \Gamma_w^2}} < M_e < \min\left(\frac{\cos \theta}{\nu_{\rm A}}, \sqrt{\frac{\nu_1 + \nu_2}{2 + 2\nu_{\rm A}^2 \Gamma_w^2}}\right), \quad (24)$$

where

$$\nu_1 = 2\cos^2\psi + (1 + v_A^2)\Gamma_w^2 
\nu_2 = \sqrt{(1 - v_A^2)^2\Gamma_w^4 - 4(1 - \cos^2\psi)(1 - v_A^2\cos^2\psi)\Gamma_w^2}.$$
(25)

Note that the condition  $M_e < \cos \theta / v_A$  is equivalent to the obvious requirement v < 1. The condition  $M_e > \cos \psi$  in

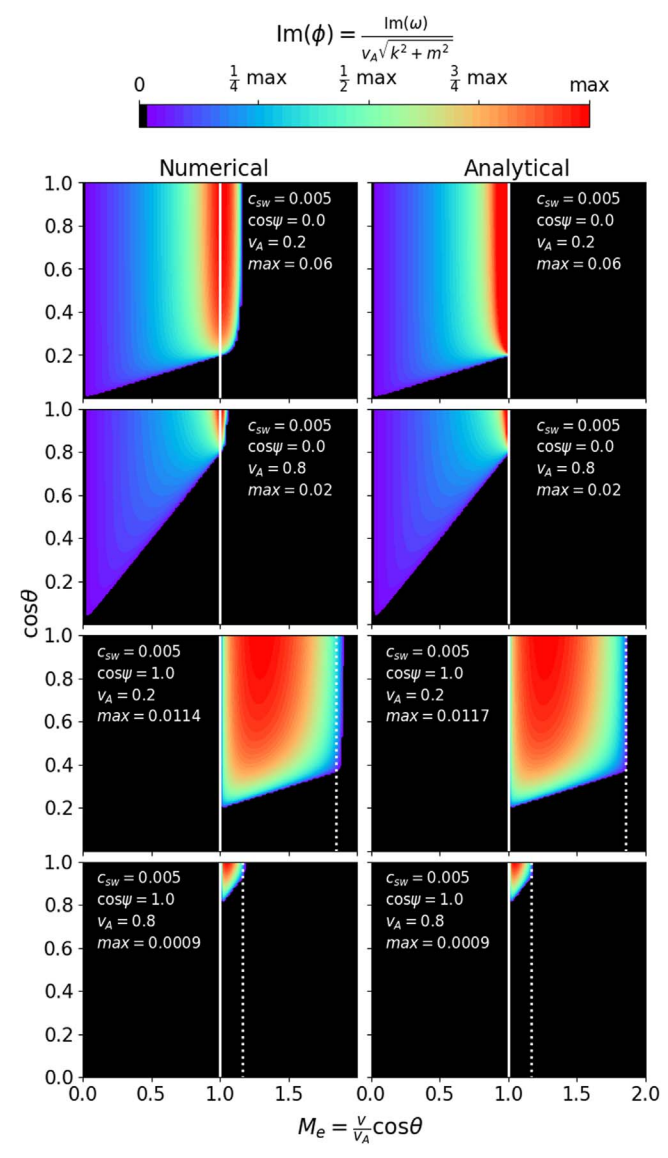


**Figure 2.** Dependence of the instability growth rate  $\text{Im}(\phi)$  on  $\theta$  and  $M_e$ , for two choices of  $v_A$  and two choices of  $\cos \psi$ , as indicated in the plots. The left and right columns represent the numerical and analytical solutions, respectively. For  $\cos \psi = 0$ , the maximum growth rate of the analytical solution is capped at its numerical counterpart to avoid the divergence at  $M_e = 1$ . In all the panels,  $\text{Im}(\phi)$ is then normalized to its maximum value, which is quoted in the panels themselves. The vertical dotted lines show the analytical upper bound on  $M_e$  when  $\cos \psi = 1$ ; see Equation (26). The vertical solid white lines indicate  $M_e = 1$ .

Equation (23) can be equivalently cast as  $v \cos \theta > v_A \cos \psi$ , which has a simple interpretation. The system is unstable if the projection of the shear velocity onto the direction of  $q_{\parallel}$  (which we defined as the projection of the wavevector q on the x-zplane; see Figure 1) is larger than the projection of the Alfvén speed onto the same direction. In other words, the shear is able to overcome magnetic tension.

Equations (23) and (24) fully characterize the instability boundaries in Figures 2 and 3. In particular, the vertical white dotted lines in the figures illustrate the upper bound in Equation (24) for the special case  $\cos \psi = 1$ , which yields

$$1 < M_e < \min\left(\frac{\cos\theta}{v_A}, \sqrt{\frac{1+\Gamma_w^2}{1+v_A^2\Gamma_w^2}}\right) \text{ for } \cos\psi = 1.$$
 (26)

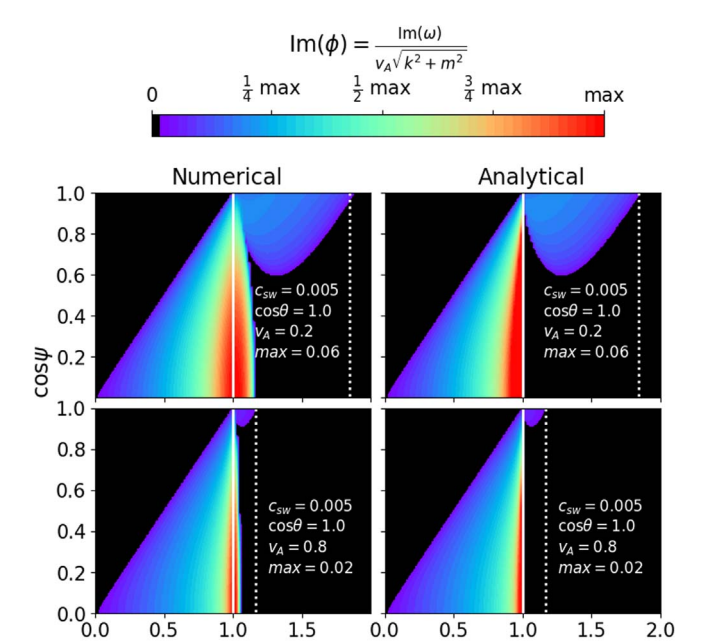


**Figure 3.** Dependence of the instability growth rate  $\text{Im}(\phi)$  on  $\psi$  and  $M_e$ , for two choices of  $v_A$  as indicated in the plots. We fix  $\cos \theta = 1$ . See the caption to Figure 2 for further details.

0.0

 $M_e = \frac{V}{V_A} \cos\theta$ 

0.5

1.5

2.0

1.0

1.5

1.0

0.5

It follows that the unstable range at  $M_e > 1$  shrinks for  $v_A \to 1$ , but never disappears as long as  $v_A < 1$ .

4.1. The Special Case 
$$M_e = 1$$

In the case  $M_e = 1$ , our analytical approximation diverges. The singular case  $M_e = 1$  can be solved by expanding  $\phi$  with a Puiseux series (Wall 2004; Wolfram Research 2020). Among the six approximate solutions of  $\phi$  at  $M_e = 1$ , the only unstable one is

$$\phi_{(M_e=1)} = 1 + (-1)^{2/3} (2\xi)^{1/3} \epsilon^{2/3}, \tag{27}$$

where

$$\xi = \frac{(\cos^2 \psi - 1)^2 (\cos^2 \theta - v_A^2)}{\Gamma_w^2 \cos^2 \theta}.$$
 (28)

In Appendix A, we demonstrate that this analytical approximation for the special case  $M_e = 1$  is in good agreement with the numerical solution.

Equation (27) allows us to identify the range of  $M_e$  (near unity) where the diverging growth rate in Equation (19) should rather be replaced by Equation (27). By equating the imaginary parts of  $\phi_{(M_e<1)}$  in Equation (19) and  $\phi_{(M_e=1)}$  in Equation (27), and solving for  $M_e$ , we can obtain the upper bound  $M_e^*$  for Equation (19) such that  $\phi_{(M_e<1)} \leqslant \phi_{(M_e=1)}$  for  $M_e \in [0, M_e^*]$ . We expect  $M_e^*$  to be close to unity, so we assume  $M_e = 1$  in  $\mu$ and  $\lambda$  for  $\Lambda_+$  of Equation (19). The resulting expression for  $M_e^*$ can then be written as

$$M_e^* = \sqrt{1 - 8 \cdot 3^{-1} (2\xi)^{1/3} \epsilon^{2/3}},$$
 (29)

where we require  $\epsilon < 3^{3/2}2^{1/5}\xi^{-1/2}$  for real  $M_e^*$ .

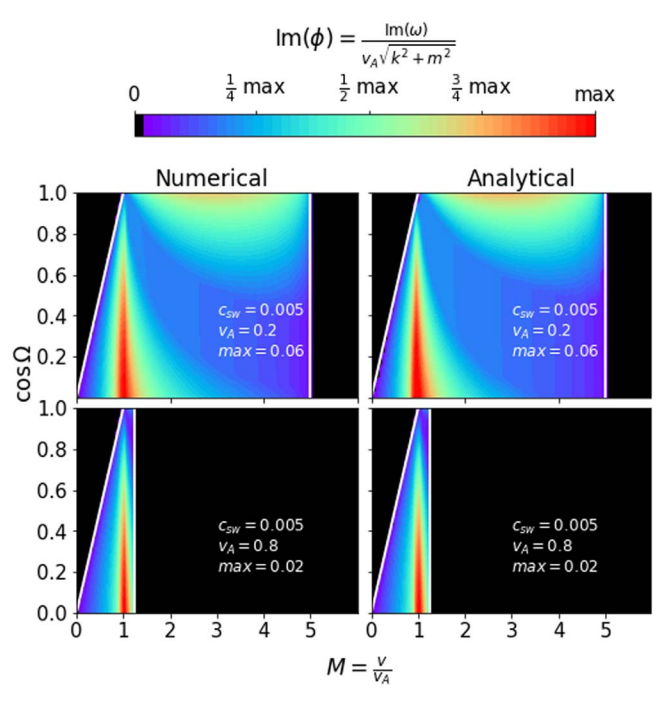


Figure 4. Dependence of the maximum instability growth rate  $\operatorname{Im}(\phi)$  on  $\cos\Omega$  and  $M \equiv v/v_A$ , for two choices of  $v_A$ , as indicated in the plots. The maximum value of  $\operatorname{Im}(\phi)$  is taken across all values of  $\cos\theta \in [0,1]$  for each  $(M,\cos\Omega)$  pair. The left and right columns represent the numerical and analytical solutions, respectively. In all the panels,  $\operatorname{Im}(\phi)$  is then normalized to its maximum value, which is quoted in the panels themselves. The white lines indicate  $M = \cos\Omega$  and  $M = 1/v_A$ .

#### 4.2. Maximum Growth Rate

The results presented so far retain the explicit dependence on the angle  $\theta$  between the projected wavevector  $\mathbf{q}_{\parallel}$  and the flow velocity  $\mathbf{v}$ , and on the angle  $\psi$  between  $\mathbf{q}_{\parallel}$  and the magnetic field  $\mathbf{B}$  (see Figure 1). In practice, for a given Mach number  $M=v/v_{\rm A}$  and a fixed magnetic field orientation (e.g., with respect to the shear direction), one can determine the maximum growth rate, irrespective of the specific value of  $\theta$  at which it is attained. This is presented in Figure 4, where we show the peak growth rate as a function of M and  $\cos \Omega$ , where we define

$$\cos\Omega = \frac{\mathbf{v} \cdot \mathbf{B}}{|\mathbf{v}||\mathbf{B}|}.\tag{30}$$

The plot shows that, for most magnetic field orientations, the peak growth rate is achieved at  $M \sim 1$ . The exception is the case of fields nearly aligned with the shear velocity, where magnetic tension pushes the unstable region to higher M. The region of stability in the upper left corner is delimited by  $M = \cos \Omega$  (the white line), which comes from the instability condition  $M_e > \cos \psi$  in Equation (23). The range of unstable Mach numbers extends up to  $M < 1/\nu_A$  (the vertical white line), which simply corresponds to the requirement  $\nu < 1$ .

#### 5. Comparison to the Hydrodynamic Case

When the unstable mode propagates perpendicular to the magnetic field ( $\cos \psi = 0$ ), we expect magnetic tension to have no effect, and the solution should resemble the hydrodynamic asymmetric case discussed by Blandford & Pringle (1976). We demonstrate this by choosing a different parameterization in Equation (16), similar to the one of Equation (2) in Blandford

& Pringle (1976), i.e.,

$$\begin{split} \epsilon' &= \frac{1}{\epsilon} = \frac{v_{\mathrm{A}}}{c_{\mathrm{sw}}}, \quad \phi' = \frac{\phi}{\epsilon} = \frac{\omega}{c_{\mathrm{sw}} \sqrt{k^2 + m^2}}, \\ \delta' &= \frac{w_{0w}}{w_{0j}^*} \frac{c_{\mathrm{sw}}^2}{v_{\mathrm{A}}^2}, \quad \eta' = v_{\mathrm{A}} \epsilon = c_{\mathrm{sw}}, \\ M' &= \frac{M \cos \theta}{\epsilon} = \frac{v}{c_{\mathrm{sw}}} \frac{k}{\sqrt{k^2 + m^2}}, \end{split}$$

where  $w_{0j}^*$  is the total enthalpy of the jet, namely the sum of the gas enthalpy  $w_{0j}$  and the magnetic enthalpy:

$$w_{0j}^* = B_{0x}^2 + B_{0z}^2 + w_{0j} = \frac{w_{0j}}{1 - v_A^2}.$$
 (31)

Then the dispersion relation Equation (16) can be equivalently written as

$$(\phi'^2 - \cos^2 \psi)^2 [\gamma^2 (1 - \eta'^2)(\phi' - M')^2 + \eta'^2 \phi'^2 - 1]$$
  
=  $\gamma^4 \delta'^2 (\phi' - M')^4 (\phi'^2 - \epsilon'^2) \epsilon'^2$ ,

which, by setting  $\cos \psi = 0$ , is exactly the same as Equation (1) in Blandford & Pringle (1976), where both the jet and the wind were assumed to be unmagnetized. We conclude that, even though our jet is magnetized, in the case  $\cos \psi = 0$ , the instability behaves similarly to the case of a hydrodynamic jet. Here, the magnetic field provides pressure, but not tension.

#### 6. Discussion and Conclusions

We have studied the linear stability properties of the KHI for relativistic, asymmetric, magnetized flows, with a focus on conditions appropriate for the interface between a magnetized relativistic jet and a gas-pressure-dominated wind. We derive the most general form of the dispersion relation and provide an analytical approximation of its solution for  $\epsilon = c_{\rm sw}/v_{\rm A} \ll 1$ . The stability properties are chiefly determined by the angle  $\psi$ between the jet magnetic field and the wavevector projection onto the jet/wind interface. For  $\psi = \pi/2$ , magnetic tension plays no role, and our solution resembles the one of a gaspressure-dominated jet. Here, only sub-Alfvénic jets are unstable  $(0 < M_e \equiv (v/v_A)\cos\theta < 1$ , as long as v < 1). For  $\psi = 0$ , the velocity shear needs to overcome the magnetic tension, and only super-Alfvénic jets are unstable  $(1 < M_e < \sqrt{(1 + \Gamma_w^2)/(1 + v_A^2 \Gamma_w^2)})$ . At zeroth order in  $\epsilon$ , the phase speed of unstable modes is  $\omega/k = v$  in the jet frame, i.e., they are purely growing in the wind frame.

Our analytical results are valuable for both theoretical and observational studies. They can be easily incorporated into global MHD simulations of jet launching and propagation, to identify KH-unstable surfaces (Chatterjee et al. 2020; Sironi et al. 2021; Wong et al. 2021). On the observational side, claims have been made that the KHI is observed along active galactic nucleus (AGN) jets, based on the geometry of the outflow (Lobanov & Zensus 2001; Issaoun et al. 2022). Our formulae can place this claim on solid grounds, if estimates of the field strength and orientation and of the flow velocities are available. Besides AGNs, our results have implications for other jetted sources, such as, but not limited to, gamma-ray bursts, tidal disruption events, X-ray binaries, and pulsar wind nebulae.

We conclude with a few caveats. First, the plane-parallel approach we employed is applicable only if the jet/wind interface

is much narrower than the jet radius (for studies of surface instabilities in force-free cylindrical jets, see, e.g., Bodo et al. 2013, 2016, 2019; Sobacchi & Lyubarsky 2018). Second, our local description implicitly assumes that the flow properties do not change as the KHI grows. Third, we have assumed the jet plasma to be cold, and the surrounding medium to be unmagnetized. These assumptions will be relaxed in a future work.

#### Acknowledgments

We are grateful to R. Narayan for many inspiring discussions and collaboration on this topic. We would like to thank G. Bodo for many useful discussions and suggestions. L.S. acknowledges support from the Cottrell Scholars Award and the DoE Early Career Award DE-SC0023015. L.S and J.D. acknowledge support from NSF AST-2108201, NSF PHY-1903412, and NSF PHY-2206609. J.D. is supported by a Joint Columbia University/ Flatiron Research Fellowship, and research at the Flatiron Institute is supported by the Simons Foundation.

# Appendix A Analytical Approximation for $M_e = 1$

For the singular case  $M_e = 1$ , our analytical solutions take the form of the first-order Puiseux series. Here, we compare the analytical and numerical solutions. In Figures 5 and 6, we plot the

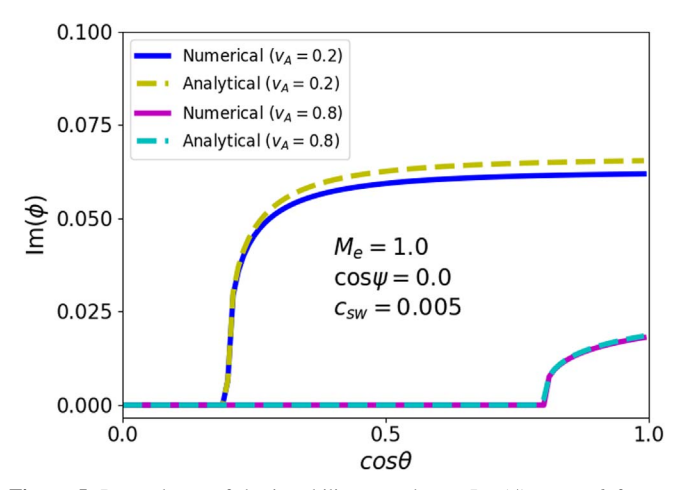


**Figure 5.** Dependence of the instability growth rate Im  $(\phi)$  on  $\cos \theta$  for two choices of  $v_A$  and a fixed value of  $\cos \psi = 0$  in the singular case  $M_e = 1$ . The solid lines represent the numerical solutions, while the dashed lines represent the analytical solutions obtained by Puiseux series expansion in the main text.

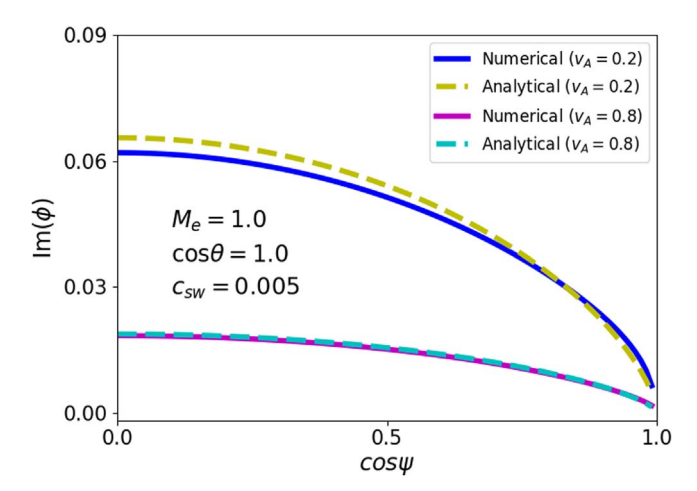


**Figure 6.** Dependence of the instability growth rate Im  $(\phi)$  on  $\cos \psi$  for two choices of  $v_A$  and a fixed value of  $\cos \theta = 1$  in the singular case  $M_e = 1$ . The solid lines represent the numerical solutions, while the dashed lines represent the analytical solutions obtained by Puiseux series expansion in the main text.

instability growth rate for  $M_e=1$ , comparing analytical and numerical solutions. We choose the same parameters as in the figures of the main paper, namely  $c_{\rm sw}=0.005$  and  $v_{\rm A}=0.2$  or 0.8. We fix  $\cos\psi=0$  for Figure 5 and  $\cos\theta=1$  for Figure 6. We use solid and dashed lines to represent numerical and analytical solutions, respectively. The figures show that our analytical solutions in Puiseux series provide a good approximation to the numerical ones across the entire range of  $\cos\theta$  (for Figure 5) and  $\cos\psi$  (for Figure 6).

# Appendix B The Second-order Terms

In the main body of the paper, we have looked for an analytical approximation of the form  $\phi \approx c_0 + c_1 \epsilon + c_2 \epsilon^2$ , where  $c_0$ ,  $c_1$ , and  $c_2$  are constant with respect to  $\epsilon$  and terms higher than  $\epsilon^2$  are ignored. For the unstable solutions, we find that the first-order term  $\Lambda_{\pm}\epsilon$  generally provides a good approximation of the numerical solution. However, the second-order term  $\Sigma_{\pm}\epsilon^2$  is required for identifying the physical solutions that satisfy the Sommerfeld condition. The explicit expression for  $\Sigma_+$  is

$$\Sigma_{\pm} = \frac{M_e \mu \left[ (1 - M_e^2) (\cos^2 \psi (1 - v_A^2) + M_e^2 (1 + 3v_A^2) - 2 - 2M_e^4 v_A^2) \Gamma_w^2 + 2(\cos^2 \psi + M_e^2 - 2)(\mu^2 \pm \lambda) \right]}{\gamma^2 (1 - M_e^2)^2 \Gamma_w^2 \lambda}.$$
 (B1)

#### ORCID iDs

Anthony Chow https://orcid.org/0000-0003-3535-6392

Jordy Davelaar https://orcid.org/0000-0002-2685-2434

Michael E. Rowan https://orcid.org/0000-0003-2406-1273

Lorenzo Sironi https://orcid.org/0000-0002-1227-2754

#### References

```
Abel, N. H. 1826, JRAM, 1826, 65
Berlok, T., & Pfrommer, C. 2019, MNRAS, 485, 908
Blandford, R. D., & Pringle, J. E. 1976, MNRAS, 176, 443
Blandford, R. D., & Znajek, R. L. 1977, MNRAS, 179, 433
Blumen, W., Drazin, P. G., & Billings, D. F. 1975, JFM, 71, 305
Boccardi, B., Krichbaum, T. P., Bach, U., et al. 2016, A&A, 585, A33
Bodo, G., Mamatsashvili, G., Rossi, P., & Mignone, A. 2013, MNRAS,
Bodo, G., Mamatsashvili, G., Rossi, P., & Mignone, A. 2016, MNRAS,
   462, 3031
Bodo, G., Mamatsashvili, G., Rossi, P., & Mignone, A. 2019, MNRAS,
   485, 2909
Bodo, G., Mignone, A., & Rosner, R. 2004, PhRvE, 70, 036304
Chandrasekhar, S. 1961, Hydrodynamic and Hydromagnetic Stability (Oxford:
  Clarendon)
Chatterjee, K., Markoff, S., Tchekhovskoy, A., et al. 2020, AAS Meeting, 235,
   411.05
Fermi, E. 1949, PhRv, 75, 1169
Ferrari, A., Trussoni, E., & Zaninetti, L. 1978, A&A, 64, 43
Ferrari, A., Trussoni, E., & Zaninetti, L. 1980, MNRAS, 193, 469
Hamlin, N. D., & Newman, W. I. 2013, PhRvE, 87, 043101
```

Issaoun, S., Wielgus, M., Jorstad, S., et al. 2022, ApJ, 934, 145

Kivelson, M. G., & Zu-Yin, P. 1984, P&SS, 32, 1335

```
Lobanov, A. P., & Zensus, J. A. 2001, Sci, 294, 128
Lord Kelvin 1871, PMag, 42, 362
Mignone, A., Mattia, G., & Bodo, G. 2018, PhPl, 25, 092114
Osmanov, Z., Mignone, A., Massaglia, S., Bodo, G., & Ferrari, A. 2008, A&A,
  490, 493
Pimentel, O. M., & Lora-Clavijo, F. D. 2019, MNRAS, 490, 4183
Prajapati, R. P., & Chhajlani, R. K. 2010, PhPl, 17, 112108
Pu, Z.-Y., & Kivelson, M. G. 1983, JGR, 88, 841
Rieger, F. M. 2019, Galax, 7, 78
Rowan, M. E. 2019, PhD thesis, Harvard Univ.
Sharma, P. K., & Chhajlani, R. K. 1998, PhPl, 5, 625
Sironi, L. 2022, PhRvL, 128, 145102
Sironi, L., Rowan, M. E., & Narayan, R. 2021, ApJL, 907, L44
Sironi, L., & Spitkovsky, A. 2014, ApJL, 783, L21
Sobacchi, E., & Lyubarsky, Y. E. 2018, MNRAS, 473, 2813
Sommerfeld, A. 1912, Jahresbericht der Deutschen Mathematiker-Vereinigung,
  21, 309
Turland, B. D., & Scheuer, P. A. 1976, MNRAS, 176, 421
Von Helmholtz, H. 1868, Monatsberichte der Königlichen Preussische
   Akademie des Wissenschaften zu Berlin, 23, 215
Walker, R. C., Hardee, P. E., Davies, F. B., Ly, C., & Junor, W. 2018, ApJ,
  855, 128
Wall, C. T. C. 2004, Puiseux' Theorem (Cambridge: Cambridge Univ.
  Press), 15
Wang, J.-S., Reville, B., Liu, R.-Y., Rieger, F. M., & Aharonian, F. A. 2021,
   MNRAS, 505, 1334
Wang, J.-S., Reville, B., Mizuno, Y., Rieger, F. M., & Aharonian, F. A. 2023,
  MNRAS, 519, 1872
Wolfram Research 2020, AsymptoticSolve, https://reference.wolfram.com/
  language/ref/AsymptoticSolve.html
Wong, G. N., Du, Y., Prather, B. S., & Gammie, C. F. 2021, ApJ, 914,
Zhang, H., Sironi, L., & Giannios, D. 2021, ApJ, 922, 261
```